physica status solidi (a)

PERSPECTIVE OPEN ACCESS

Challenges in Simultaneous Microstructuring and Hyperdoping of Germanium with Ultrafast Laser

Dmytro Gnatyuk[1] | Sara Hamed[2] | Masoud Ebrahimzadeh[3] | Hanchen Liu[1] | Ville Vähänissi[1] | Pekka Laukkanen[3] | Hele Savin[1] | Xiaolong Liu[1]

[1]Department of Electronics and Nanoengineering, Aalto University, Espoo, Finland | [2]Department of Chemistry and Materials Science, Aalto University, Espoo, Finland | [3]Department of Physics and Astronomy, University of Turku, Turku, Finland

Correspondence: Xiaolong Liu (xiaolong.liu@aalto.fi)

Received: 19 November 2025 | **Revised:** 26 January 2026 | **Accepted:** 24 March 2026

Keywords: femtosecond laser | germanium | hyperdoping | microstructuring | sub-bandgap absorption

ABSTRACT

Germanium's compatibility with Complementary Metal-Oxide-Semiconductor (CMOS) and strong near-infrared response make it an attractive platform for infrared photonics, but its intrinsic material properties hinder straightforward extension of absorption beyond the band edge. In this perspective, we synthesize recent and new experiments and analyses on femtosecond-laser approaches that attempt to combine surface microstructuring and hyperdoping of Ge in a single step. We argue that, unlike silicon, Ge's high optical absorption at visible/green wavelengths, shallow energy deposition, lower melting point, and reduced thermal conductivity favor intense localized heating, evaporation, and redeposition—conditions that both produce high baseline sub-bandgap absorption from damage and prevent effective incorporation of thin-film dopant precursors. In a case example, Ti shows only trace incorporation from qualitative measurements. We discuss why laser-induced structural disorder, rather than stable deep dopant incorporation, dominates the optical response, and we outline practical pathways forward: exploring longer wavelengths or gas-phase chemistries, applying separate in situ heating, or decoupling texturing from heavy doping.

1 | Introduction

For infrared detection, materials such as HgCdTe, InSb, and PbSe dominate due to their narrow or composition-tunable bandgaps and high detectivity; however, their reliance on complex epitaxial growth, cryogenic cooling, material toxicity, and limited CMOS compatibility imposes significant constraints on large-scale, low-cost deployment [1]. In contrast, Ge offers a unique balance between performance and manufacturability, particularly for short-wavelength and band-engineered extended short-wavelength infrared (SWIR, 1–3 μm) applications, where room temperature operation, wafer-scale processing, and monolithic integration with Si electronics are critical [2–4]. Intrinsically, Ge is limited by its indirect bandgap (0.67 eV, ∼1880 nm), resulting in insufficient optical absorption beyond the band edge and poor light coupling in planar device geometries. Consequently, approaches that can simultaneously trigger sub-bandgap absorption and enhance optical coupling, while preserving CMOS compatibility, are of particular interest.

Heavily doped or hyperdoped Ge has recently garnered attention as a promising solution to overcome the bandgap limitations, making it particularly suitable for SWIR applications and beyond [5–9]. Heavy doping enables Ge to absorb lower-energy photons, normally beyond the reach of undoped Ge, through a combination of several mechanisms. Firstly, the addition of dopant atoms leads to the creation of impurity states that can overlap and form an impurity band in the forbidden gap [10]. Secondly, interactions between the dopants and the host lattice, including exchange and correlation effects, further modify the band structure, contributing to the gap narrowing [11]. Thirdly, the incorporation of dopants induces strain in the crystal lattice, causing shifts in the band structure [12]. Recent work on hyperdoped Ge has demonstrated a noticeable photoresponse at room temperature extending into the

3.0 µm wavelength range, with a comparable absorption coefficient to those of commercial low-bandgap SWIR III–V and II–VI materials [8]. However, the techniques used to achieve hyperdoped Ge typically involve ion implantation with a thin doping layer and a flat surface, resulting in relatively low sub-bandgap absorption, typically less than 7% over 2–3 µm [7, 8]. While the material may exhibit a high absorption coefficient due to heavy doping, this alone is insufficient for practical applications. Efficient coupling of incident light into the material is also essential, and the planar geometry leads to significant reflectance losses that undermine the material's full optical potential [13]. Ideally, both hyperdoping and surface texturing would be addressed simultaneously to enhance light coupling and absorption more efficiently and economically.

A promising route to address the above issue is to use ultrafast-laser-based hyperdoping, conventionally used for hyperdoping Si. Unlike other hyperdoping approaches, ultrafast laser processing has been widely considered as a potentially synergistic pathway, in which nonequilibrium dopant incorporation and surface texturing could emerge concurrently from the same transient laser–matter interaction. This approach has successfully incorporated elements such as chalcogens (S, Se, Te) [14–17] and transition metals (e.g., Au, Ti, Cr, Mo) [18–22] far beyond their solid solubility limits into Si. Our previous work indicated that this approach could be effective for Ge as well, as femtosecond laser irradiation of Ge with a Ti dopant precursor film clearly enhanced sub-bandgap absorption compared to samples without the film [13]. Although these preliminary results are promising relative to ion-implanted Ge, further investigation is needed to fully understand and optimize the underlying doping and absorption mechanisms, as well as the associated processing conditions. Moreover, post-processing steps, such as solvent cleaning to remove laser-induced debris and thermal annealing to activate dopants and repair crystal damage, play a crucial role in tailoring the final material performance and should be systematically investigated.

In this perspective, we first discussed the complexity of the hyperdoping based on existing work and the rationale for selecting the dopant. We then present experimental results on exploring the simultaneous doping and microstructuring of Ge using femtosecond laser processing in the presence of a Ti precursor film, complemented by post-processing techniques such as solvent cleaning and rapid thermal annealing (RTA). Through comparative analysis of Ti-coated and bare Ge samples subjected to identical laser conditions, we examine sub-bandgap absorption enhancements via spectrophotometry while characterizing surface morphology evolution with scanning electron microscopy (SEM) and probing potential structural modifications using Raman spectroscopy, X-ray diffraction (XRD), and X-ray photoelectron spectroscopy (XPS). Furthermore, we discuss the mechanisms in laser-induced doping and microstructure formation in Ge through experimental evidence and comparison with Si-related studies. Looking ahead, we speculate on strategies to mitigate these challenges to achieve tailored surface texturing and dopant profiles for superior infrared optoelectronic performance.

2 | The Choice of Dopants

A wide range of dopants has been incorporated into Si at supersaturated concentrations using nonequilibrium techniques, most notably femtosecond-laser processing and ion implantation, which are summarized by numerous review articles [23–27]. Interestingly, sub-bandgap responsivity often appears in hyperdoped Si regardless of which dopant is introduced. The exact mechanisms remain debated due to the complexity of the materials and may come from deep-level dopant states, process-induced defect states, impurity-band formation, band tailing, light-trapping structures, or a combination of the above. Therefore, the term 'hyperdoping' is sometimes used loosely for any supersaturated dopant process. The femtosecond laser processing is especially messy as it often results in very high responsivity that cannot be explained purely by the intermediate band formation, but from textured surfaces, photoconductive gain, carrier trapping, avalanche-like processes, etc.

Hyperdoping in Ge has been explored far less extensively than in Si. Most reported studies focus on conventional dopants or elements with relatively high equilibrium solubility in Ge, such as B [6], Ga [28], Al [29], P [30], and As [31], primarily for applications including low-temperature superconductivity [6, 28], high-conductivity contacts [29, 31], and strain–doping band engineering [5].

For sub-bandgap photodetection, only a limited set of dopants has been investigated to date. The materials of choice have included chalcogens (S [32], Se [9], Te [7, 33]) and a few transition or noble metals (e.g., Au [8, 10]), almost exclusively incorporated through ion implantation followed by pulsed-laser melting or flash-lamp annealing. Although these approaches reliably achieve supersaturated concentrations, the resulting sub-bandgap absorptance and device responsivity have remained moderate, often constrained by dopant clustering, residual defects, and shallow modified layers.

The femtosecond-laser hyperdoping of Ge has been scarcely studied, with virtually no prior systematic work before our recent demonstration [13], despite its potential to simultaneous surface texturing and hyperdoping for broadband absorption enhancement. We primarily selected Ti as the dopant because it is widely used in microelectronics and contact metallization, is nontoxic and earth-abundant, and has already been successfully incorporated into Si to demonstrate extended sub-bandgap responsivity [34] and even carrier-lifetime enhancement [35].

Unfortunately, the fundamental properties of Ti in Ge are only sparsely documented. A data article report the maximum equilibrium solubility limit of Ti in Ge to be 2.3% in atomic ratio [36], but it might be a misinterpretation of the eutectic point from Ge–Ti phase diagram [37, 38]. Ti is a Group-IV transition metal with four valence electrons, nominally matching the valence electron count of Ge. Due to the differences in orbital energy, Ti can produce deep localized states inside the bandgap. Previous deep-level transient spectroscopy (DLTS) studies [39] have shown that substitutional Ti in Ge introduces two well-defined deep electronic states: an electron trap (Ti-E1, $E_C - 0.228$ eV) in n-type material and a hole trap (Ti-H1, $E_V + 0.025$ eV) in p-type material. The presence of these mid-gap states suggests that Ti hyperdoping could, in principle, support the formation of intermediate bands.

Nevertheless, beyond these DLTS measurements, very little is known, experimentally or theoretically, about Ti solubility, diffusion behavior, electronic activity, or defect configurations in Ge. Modeling transition-metal impurities in narrow-bandgap semiconductors such as Ge is intrinsically demanding [40–42]. Beyond the well-known bandgap underestimation of standard density functional theory (DFT), there are also significant practical constraints that limit the accuracy and feasibility of first-principles defect calculations. Reliable defect calculations typically require very large supercells to minimize spurious defect–defect interactions and simulate smaller dopant concentrations, which in turn leads to substantially increased computational cost and prohibitively long simulation times when using hybrid or beyond-DFT methods. As a result, obtaining quantitatively trustworthy defect energetics and level positions in these systems remains computationally intensive and technically challenging.

Despite these uncertainties, Ti remains a worthwhile candidate to explore experimentally. As mentioned earlier, in Si, a diverse range of hyperdoped species, regardless of their original intended role, have consistently produced measurable sub-bandgap response, often through mechanisms that extend beyond the idealized 'intermediate-band' picture. This suggests that evaluating Ti in Ge may similarly reveal useful sub-bandgap absorption pathways, whether arising from impurity-band formation, defect-assisted transitions, or other nonequilibrium doping effects.

3 | Experimental Results

The schematic illustration of the fabrication process for microstructured and hyperdoped Ge is presented in Figure 1a, with the detailed experimental procedure documented in Supplementary Material. Pristine Ge wafer is either coated with Ti as dopant precursor or left uncoated as reference. The Ti precursor thickness was fixed at 50 nm, as prior optimization showed no further improvement in sub-bandgap absorption for thicker films [13]. They are processed later with identical conditions to maintain consistent surface morphology and minimize the influence of scattering on the optical measurements for comparing the two samples. We emphasize that, unlike in our earlier study [13], a solvent-cleaning step is introduced before the RTA to remove laser-generated debris, thereby reducing ambient contamination. This procedure is a typical practice for laser-processed Si.

Figure 1b shows the total absorptance spectra (1900–2500 nm) of bare (dashed line) and Ti-coated (solid line) Ge samples after each processing step. Although the incorporation of Ti increases absorptance, the difference is unexpectedly small (<3%) after both laser processing and solvent cleaning. The difference becomes smaller with increasing annealing temperatures (Figure S1 in Supplementary Material) and at 600°C the absorptance of Ti-coated sample even falls below the reference sample. These marginal variations fall within experimental uncertainty and do not indicate a systematic effect associated with Ti coating. Furthermore, the change in absorptance appears to be more strongly influenced by the processing conditions than by the presence of doping (with or without Ti coating) alone. Naturally, the key questions arising from the unexpected results are how processing steps affect the surface morphology, whether Ti is effectively incorporated into the microstructures, and what dominates the sub-bandgap absorption mechanism that may be inferred after laser and post-laser processing.

To address these questions, we first use SEM to confirm that a dense, irregular array of microconical structures forms on the Ge surface after laser processing (Figure S2 in Supplementary Material), which are known to effectively reduce surface reflection. The morphology of the microstructures remains largely unchanged with or without the Ti film, for thicknesses up to 150 nm [13]. However, post-laser processing steps significantly alter the surface morphology, as illustrated in Figure 2a, which shows the Ti-coated surface after laser processing, subsequent solvent cleaning, and final RTA at 600°C, respectively. Post-laser processing alters the surface roughness of the microstructures: solvent cleaning effectively removes loosely bound nanoparticles with diameters smaller than ~50 nm, while RTA also eliminates the larger nanoparticles, resulting in a smoother overall surface.

Next, we use Raman spectroscopy to examine the modifications in the crystal structure after each processing step. Figure 2b summarizes the changes in the position and full width at half maximum (FWHM) of the Ge Raman main peak, corresponding to the transverse optical (TO) phonon mode (for full spectrum refer to Figure S3 in Supplementary Material). In Figure 2b, laser

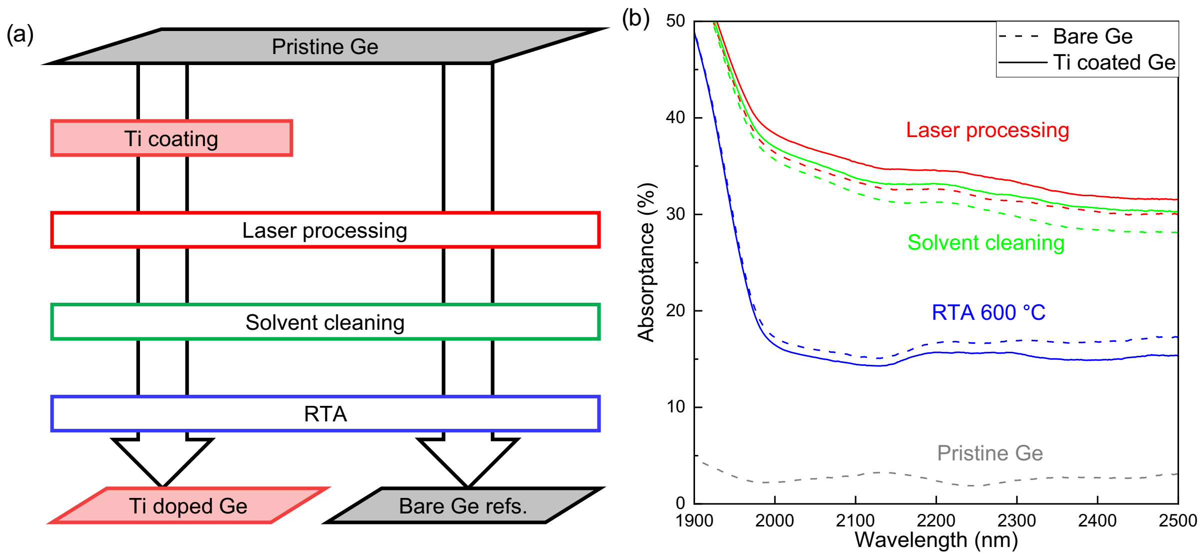

FIGURE 1 | (a) Schematic illustration of the sample fabrication process. (b) Absorptance spectra of the Ge samples with (solid lines) and without (dashed lines, bare Ge) Ti coating before (pristine Ge) and after laser processing with following solvent cleaning and RTA at 600°C.

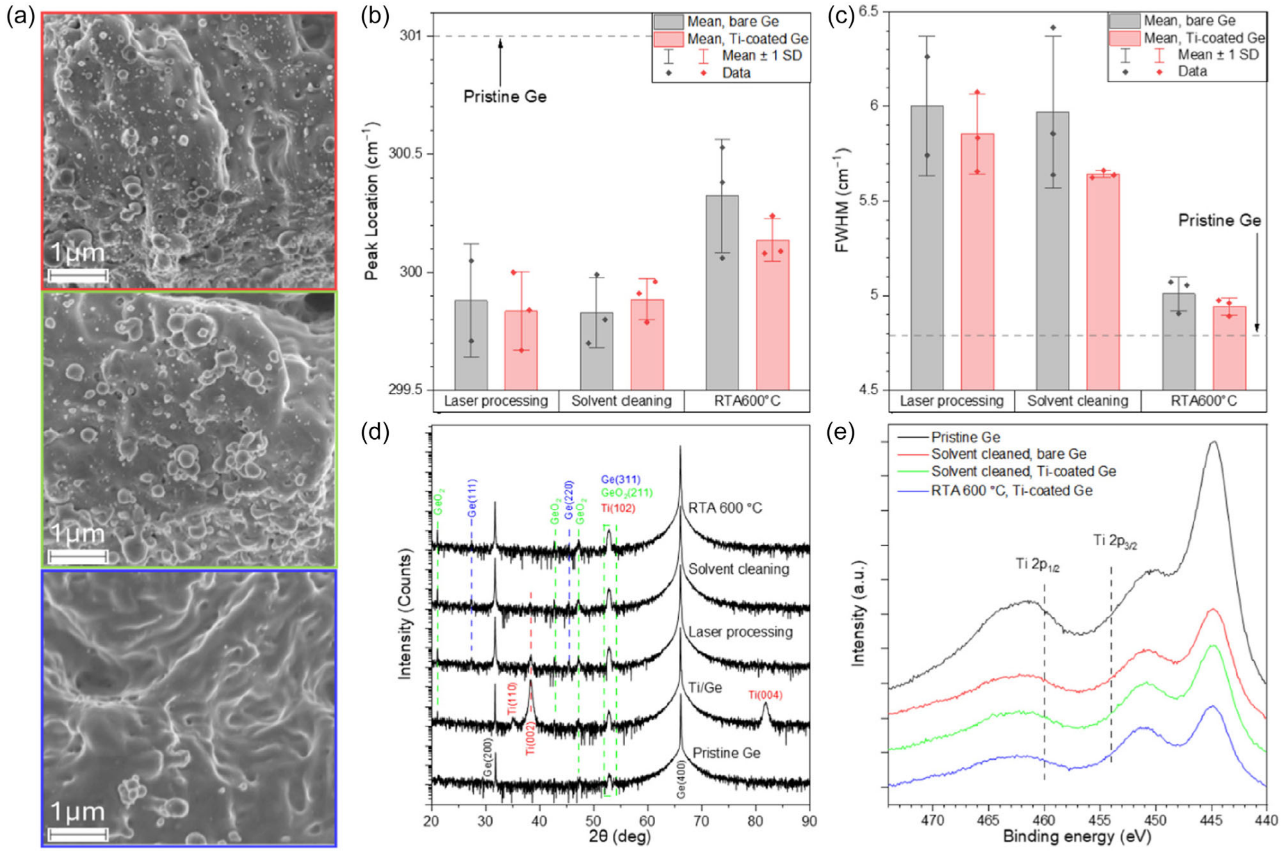

FIGURE 2 | Characterization of the fs laser microstructured Ge. (a) SEM images of the Ti-coated Ge (top to bottom) after laser processing, after solvent cleaning and after 600°C RTA. (b,c) Ge Raman mean peak location (b) and FWHM (c) for fs laser microstructured Ge with and without Ti coating compared to that measured from pristine Ge. (d) XRD patterns for Ti-coated Ge samples after each processing step with pristine Ge as reference. (e) XPS of different fs-laser-irradiated Ge samples together with a pristine Ge reference.

processing generally results in a slight redshift of the Ge Raman peak to 299.7–300.1 cm^{-1}, primarily attributed to tensile stress induced by structural defects. In Figure 2c, the observed broadening of the FWHM to 5.7–6.4 cm^{-1} is not only due to structural defects but also partly caused by the presence of amorphous Ge phases, which exhibit a broad TO mode centered around 270 cm^{-1} [9] that overlaps with the sharper TO peak of crystalline Ge. The difference between Ti-coated and uncoated samples falls within the experimental error, suggesting that the presence of Ti has a minimal impact under the current processing conditions.

After solvent cleaning, SEM observations in Figure 2a show that small surface particles are effectively removed. These features are therefore attributed to processing-related surface byproducts rather than intrinsic laser-induced bulk lattice modification. Following RTA, the Raman peak shifts closer to the characteristic position of crystalline Ge for both samples, and the FWHM decreases significantly, indicating recrystallization of the previously damaged layer and the restoration of long-range structural order. This behavior closely parallels the observed reduction in sub-bandgap absorptance, suggesting that structural disorder is the primary contributor to absorptance.

XRD spectra, acquired to evaluate laser-induced modifications in Ge crystallinity and to identify possible Ge- or Ti-related crystalline phases, are shown in Figure 2d. Note that for all spectra, the peak at ∼52.8° with similar intensity likely results from overlapping contributions of Ge (ICSD 636 526), GeO_2 (ICSD 59 624), or Ti (ICSD 192 331) phases, and therefore cannot be regarded as definitive evidence of Ti presence and is excluded from our analysis.

The pristine Ti-coated Ge (Ti/Ge) sample exhibits distinct diffraction peaks corresponding to metallic Ti in the (110), (002), and (004) orientations, in addition to prominent Ge (400) and (200) reflections, along with several peaks attributable to GeO_2-related phases; however, given the ultrashort pulse duration and the absence of direct chemical evidence for oxidation, such assignments remain tentative. Following laser processing, the intensity of the Ti diffraction peaks significantly diminishes, with only a weak (002) peak remaining; however, this residual peak nearly vanishes after subsequent solvent cleaning. These observations suggest that Ti predominantly exists as metallic Ti surface particles or residual film fragments, rather than being incorporated into the Ge lattice, and that these metallic Ti species are largely removed during solvent cleaning.

Besides metallic Ti, the trace formation of Ti–Ge intermetallic compounds (e.g., $TiGe_2$, Ti_5Ge_4, Ti_5Ge_3, Ti_2Ge) cannot be excluded, as such phases likely form under laser processing or thermal annealing in Ge-based systems [43–45]. However, their strongest diffraction peaks in the 36°–42° range would overlap with the metallic Ti features observed in Figure 2d, and thus, unambiguous phase identification is not possible. Notably, the disappearance of weak Ti-related diffraction feature assigned Ti (002) after RTA at 600°C is consistent with redistribution, dissolution, or transformation of residual Ti-containing phases from the near-surface region, whether metallic or intermetallic in nature.

Consistently, the high-resolution XPS spectra shown in Figure 2e do not exhibit any discernible Ti 2p peaks at the expected binding energy positions indicated by dashed lines [46] following either solvent cleaning or RTA, with all observed peaks (likely Auger peaks) attributable solely to pristine Ge. Additionally, there are no additional peaks in other Ti-related core-level regions such as Ti 3p when comparing these samples (Figure S4 in Supplementary Material). These results indicate that the effective Ti concentration is likely at or below the detection limit of the instrument, which is typically >0.1 at. % [47] or $>4\times10^{19}$ cm^{-3} in the case of cubic Ge. Such a low doping concentration may explain that Ti doping does not significantly contribute to sub-bandgap absorptance.

4 | Discussion and Perspective

4.1 | Hyperdoping and Microstructure Formation Mechanism

Our results clearly show that while Ge develops microstructures similar to those observed in Si, hyperdoping is not achieved using a Ti film precursor. To understand the significant deviation in results for Ge compared to femtosecond laser-hyperdoped silicon, it is essential to revisit the underlying mechanisms that govern the doping process and microstructure formation. While ultrafast laser–matter interaction involves a wide spectrum of nonequilibrium electronic, thermal, and hydrodynamic processes, a comprehensive treatment lies beyond the scope of this perspective. Instead, in the following discussion, we focus on the aspects most directly relevant to the contrasting outcomes observed here.

Laser doping is generally regarded as a transient liquid-phase epitaxial process, involving localized melting, dopant incorporation (incl. diffusion), and rapid resolidification [48]. Doping can be achieved through the introduction of dopants, either in the gaseous environment or as a coated thin film (note that Sher et al. [49] point out that surface-adsorbed molecules are the dominant source of dopants, so the thin film provides a localized dopant source).

The melting dynamics are highly dependent on specific parameters, particularly the pulse duration. During the process, laser energy rapidly heats the dopant film and a thin surface layer of the host material, causing them to melt. In the liquid phase, dopant atoms exhibit significantly higher diffusivity and solubility than in the solid state. As the laser pulse ends, the molten layer cools and solidifies rapidly, trapping dopant atoms within the crystal lattice [48].

In the case of femtosecond lasers, the pulses are so short that the laser energy is deposited faster than significant lattice heating can occur, primarily exciting electrons rather than causing thermal diffusion into the surrounding material [50]. At sufficiently high pulse fluences, nonthermal melting can take place. When a large number of valence electrons are excited into the conduction band beyond a critical threshold (e.g., $\sim10^{22}$ cm^{-3}), the lattice becomes unstable and undergoes an ultrafast transition to a liquid-like state within picoseconds, before energy transfer to the lattice occurs via electron–phonon coupling (~1–10 ps) [51, 52]. This results in the formation of a small, transient molten layer where dopant diffusion occurs. The melting is confined to an extremely thin region and for a very short duration, effectively minimizing collateral damage.

On the other hand, microstructure formation involves material removal, which can occur through both thermal and nonthermal processes, depending on the material properties and laser parameters [48]. In silicon, when the laser fluence exceeds the ablation threshold, laser-induced periodic surface structures form due to melt dynamics, as the incoming light interferes with scattered light from the material surface. With increasing pulse numbers, self-focusing effects in the valleys may lead to the development of larger and deeper structures within the material. During this process, part of the surface melts and evaporates, forming an ablation plume [53]. Some of the plume material redeposits onto the microstructures in the form of mixed crystalline and amorphous nanoparticles [54], which can be removed subsequently through chemical cleaning.

4.2 | Challenges

Compared to Si, where femtosecond laser processing can simultaneously achieve microstructure formation and hyperdoping, our results highlight that in Ge, the laser conditions required to produce similar microstructures are too intense to allow effective hyperdoping with Ti. Interestingly, this limitation arises even though the fluence applied to Ge is much lower than that typically used for Si [55]. Our XRD analysis shows, though not quantified, a higher concentration of Ti on the Ge surface before debris removal, with the debris being predominantly amorphous. This indicates that Ti was incorporated into the Ge lattice through a process of melting and resolidification. However, the laser conditions necessary for microstructure formation in Ge are so intense that they cause the temperature in the melting layer to rise significantly, resulting in evaporation or gas-phase ejection from the surface. As a result, thermal ablation is more pronounced in Ge during microstructuring compared to Si.

Key material differences may contribute to this behavior. Ge has small optical (0.67 eV for Ge versus 1.1 eV for Si) and thermal (0.26 eV for Ge versus 0.6 eV for Si) bandgaps, low melting point (1210 K for Ge versus 1681 K for Si) and low thermal conductivity (60 W m^{-1} K^{-1} for Ge versus 156 W m^{-1} K^{-1} for Si at room temperature) [56]. The reduced thermal conductivity in Ge can lead to a higher heat pileup close to the surface, while the lower melting point and lower thermal bandgap increase Ge's susceptibility to thermal and nonthermal ablation under these intense laser conditions. More importantly, Ge has a significantly higher absorption coefficient than Si, which, particularly at the used laser wavelength (520 nm), is nearly 2 orders of magnitude higher than that of Si [57]. This corresponds to an absorption depth of less than 20 nm in Ge, meaning that laser energy is deposited in a much shallower region, leading to highly localized heating, more abrupt temperature gradients, and an increased likelihood of surface evaporation or plasma formation.

It is worth noting that although sub-bandgap absorptance exceeding 70% can be achieved through laser parameter optimization [13], in this study, the laser parameters were intentionally chosen to yield relatively low sub-bandgap absorption. This decision is based on two considerations. First, as revealed by combined optical and structural analyses, most of the absorption at higher levels arises from laser-induced damage, which introduces free carrier absorption or tail-state absorption [58]—mechanisms that are undesirable for optoelectronic applications. Second, the Ti-induced enhancement of sub-bandgap absorption is more clearly distinguishable and pronounced when the baseline absorptance is low [13]. While we did not quantitatively determine the doping concentration or sub-bandgap absorption under even less intense laser conditions, we do not expect a significant difference, as inferred from the low sub-bandgap absorption improvement after incorporating Ti. In fact, one of the few studies attempting to obtain hyperdoped Ge [32] demonstrated that nanosecond-pulsed laser melting (1064 nm) in an SF_6 gas atmosphere can achieve sulfur hyperdoping with only slight surface morphology modifications. However, the resulting sulfur concentration remained relatively low ($\sim 2 \times 10^{19}$ cm^{-3} at the surface and $\sim 1 \times 10^{17}$ cm^{-3} at a depth of 10 nm) compared to S-hyperdoped Si, whereas no sub-bandgap response was reported. This further supports that the observed differences originate from the intrinsic material properties of Ge, and this behavior most likely extends to other dopant sources delivered via thin films or spin-on methods.

4.3 | Prospects

While our experiments and analysis expose significant challenges and deviations from the established paradigm of femtosecond-laser hyperdoping in silicon, they also reveal a broad and largely unexplored parameter space for germanium that warrants further investigation by the wider community. A primary limitation arises from the relatively shallow absorption depth and melt depth in Ge under the present irradiation conditions, suggesting that future optimization may benefit from longer-wavelength femtosecond irradiation (e.g., centered around 1–2 μm) to promote deeper melting and more effective dopant incorporation.

It should be noted that the current strategy relies on a Ti film, which complicates dopant incorporation: Ti has a much higher melting point than Ge, limiting incorporation during transient melting, and is prone to oxidation prior to laser annealing. A thin Ge capping layer on top of the Ti could help mitigate oxidation [29]. In addition, the pronounced evaporation of Ti during repeated laser irradiation indicates that selecting dopant species with lower melting or vaporization temperatures closer to that of Ge may help mitigate dopant loss. For example, chalcogen dopants such as Se or Te may offer improved incorporation efficiency in Ge due to their lower melting temperatures and stronger tendency to form deep-level states, while group-III elements (e.g., Ga or In) or Ge-alloying species such as Sn could further reduce dopant evaporation by virtue of their high solubility in liquid Ge.

Beyond thin-film precursors, alternative hyperdoping routes, such as gas-phase or liquid-phase dopant delivery, could further compensate for dopant depletion under high pulse accumulation. Moreover, the large number of accumulated laser pulses required for microstructuring may result in dopant incorporation during early irradiation stages followed by partial removal during subsequent ablation, suggesting that optimizing the laser processing with lower pulse numbers could be a viable strategy.

If simultaneous microstructuring and hyperdoping cannot be reliably achieved within a single laser pass, it becomes necessary to consider more sophisticated processing strategies. One potential approach is to induce in situ melting after microstructure formation, enabling dopant-bearing nanoparticles to be trapped more effectively and tolerant to solvent cleaning. This strategy is motivated by our earlier observation that sub-bandgap absorption improves markedly when nanoparticles are retained prior to RTA [13] and similar in situ approach has been adopted to anneal ultrafast laser hyperdoped Si [59]. In principle, such in situ melting could be achieved using the same femtosecond laser employed for microstructuring by carefully controlling thermal melting [60], thereby eliminating the need for a second laser source.

In addition to further laser-based optimization, another strategy to enhance sub-bandgap absorption would be to decouple microstructuring and hyperdoping. The excess thermal ablation during laser processing helps to remove the resolidification layer, which typically exhibits significant lattice distortion due to rapid cooling, leaving behind a lightly strained sublayer on the microstructure. This sublayer can be effectively recovered through subsequent thermal processing, provided that the laser conditions do not become so intense as to trigger microstructural collapse [61]. Moreover, any minor damage from this laser ablation is largely inconsequential if hyperdoping is later accomplished via ion implantation, since ion implantation generally results in complete amorphization of the affected layer when targeting for heavy doping, which can be fully crystallized after thermal annealing, flash lamp annealing or pulsed laser melting [9]. Therefore, further optimization of this decoupled approach could open new avenues in tailoring microstructures and dopant profiles independently, achieving a more precise control of both surface morphology and doping profile.

5 | Conclusion

Translating femtosecond-laser–based microstructuring and hyperdoping methods from Si to Ge is far from trivial. Our initial attempts with Ti-coated Ge indicate that the observed sub-bandgap absorption arises predominantly from laser-induced structural modification rather than from substantial dopant incorporation. Although Ti can be detected immediately after laser irradiation, it appears largely confined to surface nanostructures that are easily removed during subsequent cleaning, thus contributing little to the final sub-bandgap absorption. A comparison with Si highlights that the intrinsic material differences, particularly melting behavior and optical absorption, play a decisive role in both microstructure evolution and dopant incorporation. These insights suggest that achieving simultaneous microstructuring and effective hyperdoping in Ge with a single ultrafast-laser step may be fundamentally constrained. Moving forward, more refined strategies will be needed, including deeper optimization of laser and post-processing parameters, the use of additional in situ thermal assistance, or deliberately decoupling the doping and structuring steps to allow independent control over dopant incorporation and surface morphology.

Author Contributions

Dmytro Gnatyuk: data curation (equal); formal analysis (equal); investigation (equal); writing – original draft (equal); writing – review &

editing (equal). **Sara Hamed**: data curation (equal); investigation (equal); writing – review & editing (equal). **Masoud Ebrahimzadeh**: data curation (equal); investigation (equal); writing – review & editing (equal). **Hanchen Liu**: formal analysis (equal); investigation (equal); writing – review & editing (equal). **Ville Vähänissi**: formal analysis (equal); funding acquisition (equal); validation (equal); writing – original draft (equal); writing – review & editing (equal). **Pekka Laukkanen**: formal analysis (equal); resources (equal); supervision (equal); validation (equal). **Hele Savin**: formal analysis (equal); funding acquisition (equal); supervision (equal); validation (equal); writing – original draft (equal); writing – review & editing (equal). **Xiaolong Liu**: formal analysis (equal); funding acquisition (equal); investigation (equal); methodology (equal); resources (equal); supervision (equal); validation (equal); visualization (equal); writing – original draft (equal); writing – review & editing (equal).

Acknowledgments

The authors acknowledge the provision of facilities and technical support by Aalto University at OtaNano-Micronova Nanofabrication Centre.

Open access publishing facilitated by Aalto-yliopisto, as part of the Wiley - FinELib agreement.

Funding

This study was supported by Research Council of Finland through project HyperGer (354199), NIR-REM (365427), and PREIN (346529).

Conflicts of Interest

The authors declare no conflicts of interest.

Data Availability Statement

The datasets that support the findings of this study are openly available in Zenodo at https://doi.org/10.5281/zenodo.18845748.

References

1. B. Roy, B. Aref, and D. Mukherjee, "*A Strategic Review on MIR Photodetectors: Recent Status and Future Trends," In International Conference on Innovative Computing and Communications*, (2023), 653–664.

2. H. Liu, T. P. Pasanen, T. H. Fung, et al., "Near-Infrared Germanium PIN-Photodiodes with >1A/W Responsivity," *Light, Science & Applications* 14, no. 1 (2025): 9.

3. D. Marris-Morini, V. Vakarin, J. M. Ramirez, et al., "Germanium-Based Integrated Photonics From Near- to Mid-Infrared Applications," *Nanophotonics* 7, no. 11 (2017): 1781–1793.

4. C.-Y. Hsu, B. Lai, L. Guan-Yu, and Z. Pei, "High Detectivity Ge Photodetector at 940 nm Achieved by Growing Strained-Ge with a Top Si Stressor," *Optics Express* 32, no. 6 (2024): 10490.

5. L. He, S.-Y. Wen, Y.-H. Zhu, S.-T. Wu, and J.-W. Luo, "Hyperdoping of Germanium with Argon toward Strain-Doping-Induced Indirect-to-Direct Bandgap Transition in Ge," *Applied Physics Letters* 125 (2024): 5.

6. Y. Cheng, F. Long, O. Steuer, et al., "Milliseconds Thermal Processing of Boron Hyperdoped Germanium," *Physica Status Solidi* 221, no. 24 (2024): 2400260.

7. H. H. Gandhi, D. Pastor, T. T. Tran, et al., "Chalcogen-Hyperdoped Germanium for Short-Wavelength Infrared Photodetection," *AIP Advances* 10, no. 7 (2020): 075028.

8. H. H. Gandhi, D. Pastor, T. T. Tran, et al., "Gold-Hyperdoped Germanium with Room-Temperature Sub-Band-Gap Optoelectronic Response," *Physical Review Applied* 14, no. 6 (2020): 064051.

9. X. Liu, P. McKearney, S. Schäfer, et al., "Impact of Post-Ion Implantation Annealing on Se-Hyperdoped Ge," *Applied Physics Letters* 125, no. 4 (2024): 42102.

10. S. S. Dissanayake, N. Ferdous, H. H. Gandhi, et al., "Carrier Dynamics and Absorption Properties of Gold-Hyperdoped Germanium: Insight Into Tailoring Defect Energetics," *Physical Review Applied* 15, no. 6 (2021): 064058.

11. S. C. Jain and D. J. Roulston, "A Simple Expression for Band Gap Narrowing (BGN) in Heavily Doped Si, Ge, GaAs and GexSi1−x Strained Layers," *Solid-State Electronics* 34, no. 5 (1991): 453–465.

12. R. Camacho-Aguilera, Z. Han, Y. Cai, L. C. Kimerling, and J. Michel, "Direct Band Gap Narrowing in Highly Doped Ge," *Applied Physics Letters* 102, no. 15 (2013): 152106.

13. X. Liu, D. V. Gnatyuk, J. Halmela, V. Vähänissi, and H. Savin, "Fs-Laser Significantly Enhances Both Above- and Below-Bandgap Absorption in Germanium," *Optical Materials Express* 15, no. 2 (2025): 247–256.

14. P. Mc Kearney, S. Schäfer, X. Liu, et al., "Impact of Pulse Duration on the Properties of Laser Hyperdoped Black Silicon," *Advanced Photonics Research* 5, no. 6 (2024): 2300281.

15. H. Sun, X. Liu, L. Zhao, et al., "Mid-Long Wavelength Infrared Absorptance of Hyperdoped Silicon via Femtosecond Laser Microstructuring," *Optics Express* 30, no. 2 (2022): 1808.

16. X.-L. Liu, S.-W. Zhu, H.-B. Sun, et al., "Infinite Sensitivity" of Black Silicon Ammonia Sensor Achieved by Optical and Electric Dual Drives," *ACS Applied Materials & Interfaces* 10, no. 5 (2018): 5061–5071.

17. B. R. Tull, M. T. Winkler, and E. Mazur, "The Role of Diffusion in Broadband Infrared Absorption in Chalcogen-Doped Silicon," *Applied Physics A* 96, no. 2 (2009): 327–334.

18. Y. Yang, Z.-Y. Ren, C. Li, and J.-H. Zhao, "Sub-Bandgap Photo-Response of Mo-Hyperdoped Black Silicon MSM Photodetectors," *Optical and Quantum Electronics* 55, no. 3 (2023): 259.

19. H. Yang, X. Cai, S. Zeng, et al., "Titanium Hyperdoping of Silicon Solar Cells via Nanosecond-Plused Laser Melting and the Key Factors Affecting Their Performance," *ACS Applied Energy Materials* 8, no. 2 (2025): 1006–1019.

20. Y. Li, G. Feng, X. Liu, H. Li, B. Dong, and L. Zhao, "Au-Hyperdoped Black Silicon for Room Temperature Ammonia Gas Sensing with Enhanced Response and Stability," *Surfaces and Interfaces* 67 (2025): 106638.

21. V. Pryakhina, S. Kudryashov, M. Kovalev, E. Greshnyakov, and A. Akhmatkhanov, "Spatial Confinement in Laser-Induced Gold-Hyperdoping of Si Wafers," *Optics and Laser Technology* 188 (2025): 112945.

22. C. Li, J.-H. Zhao, Y. Yang, Q.-D. Chen, Z.-G. Chen, and H.-B. Sun, "Sub-Bandgap Photo-Response of Chromium Hyperdoped Black Silicon Photodetector Fabricated by Femtosecond Laser Pulses," *IEEE Sensors Journal* 21, no. 22 (2021): 25695–25702.

23. Z. Tong, M. Bu, Y. Zhang, D. Yang, and X. Pi, "Hyperdoped Silicon: Processing, Properties, and Devices," *Journal of Semiconductors* 43, no. 9 (2022): 093101.

24. J. Fu, D. Yang, and X. Yu, "Hyperdoped Crystalline Silicon for Infrared Photodetectors by Pulsed Laser Melting," *A Review. Physica Status Solidi* 219, no. 14 (2022): 2100772.

25. S. Huang, X. Jin, Q. Wu, et al., "Ultrafast Laser Hyperdoped Black Silicon and Its Application in Photodetectors: A Review," *Physica Status Solidi* 221, no. 24 (2024): 2400127.

26. C. Li, J.-H. Zhao, and Z.-G. Chen, "Infrared Absorption and Sub-Bandgap Photo-Response of Hyperdoped Silicon by Ion Implantation and Ultrafast Laser Melting," *Journal of Alloys and Compounds* 883 (2021): 160765.

27. M.-J. Sher and E. G. Hemme, "Hyperdoped Silicon Materials: From Basic Materials Properties to Sub-Bandgap Infrared Photodetectors," *Semiconductor Science and Technology* 38, no. 3 (2023): 033001.

28. S. Prucnal, V. Heera, R. Hübner, et al., “Superconductivity in Single-Crystalline Aluminum- and Gallium-Hyperdoped Germanium,” *Physical Review Materials* 3, no. 5 (2019): 054802.

29. E. Di Russo, E. Coccato, D. Fontana, et al., “Ex-Situ Incorporation of Al in Ge by Sputter Deposition and Pulsed Laser Melting: A New Approach to Fabricate Hyper-Doped Ge: Al Alloys,” *Applied Surface Science* 710 (2025): 163946.

30. G. M. Spataro, M. Faverzani, E. Di Russo, et al., “Hyperdoping of Ge/Si and SiGe/Si Epitaxial Layers by UV-Nanosecond Laser Processing,” *Materials Science in Semiconductor Processing* 200 (2025): 109928.

31. T. Alphazan, A. Díaz Álvarez, F. Martin, et al., “Shallow Heavily Doped n++ Germanium by Organo-Antimony Monolayer Doping,” *ACS Applied Materials & Interfaces* 9, no. 23 (2017): 20179–20187.

32. K. Sun and M. C. Gupta, “Pulse Laser Sulfur-Hyperdoping of Germanium and High Quantum Efficiency Photodiodes,” *IEEE Photonics Journal* 8, no. 5 (2016): 1–10.

33. D. Caudevilla, S. Algaidy, F. Pérez-Zenteno, et al., “Electrical Transport Properties in Ge Hyperdoped with Te,” *Semiconductor Science and Technology* 37, no. 12 (2022): 124001.

34. E. García-Hemme, D. Caudevilla, S. Algaidy, et al., “On the Optoelectronic Mechanisms Ruling Ti-Hyperdoped Si Photodiodes,” *Advanced Electronic Materials* 8 (2022): 2.

35. E. Antolín, A. Martí, J. Olea, et al., “Lifetime Recovery in Ultrahighly Titanium-Doped Silicon for the Implementation of an Intermediate Band Material,” *Applied Physics Letters* 94, no. 4 (2009): 042115.

36. R. Goodall, “Data of the Maximum Solid Solubility Limits of Binary Systems of Elements,” *Data in Brief* 26 (2019): 104515.

37. R. W. Bittner, C. Colinet, J.-C. Tedenac, and K. W. Richter, “Revision of the Ge–Ti Phase Diagram and Structural Stability of the New Phase Ge4Ti5,” *Journal of Alloys and Compounds* 577 (2013): 211–216.

38. H. Okamoto, “Ge-Ti (Germanium-Titanium),” *Journal of Phase Equilibria and Diffusion* 33, no. 4 (2012): 349.

39. J. Lauwaert, J. Van Gheluwe, J. Vanhellemont, E. Simoen, and P. Clauws, “Electronic Properties of Titanium and Chromium Impurity Centers in Germanium,” *Journal of Applied Physics* 105, no. 7 (2009): 073707.

40. E. Igumbor, C. N. M. Ouma, G. Webb, and W. E. Meyer, “Ab-Initio Study of Germanium Di -Interstitial Using a Hybrid Functional (HSE),” *Physica B: Condensed Matter* 480 (2016): 191–195.

41. R. M. Nieminen, “Issues in First-Principles Calculations for Defects in Semiconductors and Oxides,” *Modelling and Simulation in Materials Science and Engineering* 17, no. 8 (2009): 084001.

42. S. D. Mahanti, K. Hoang, and S. Ahmad, “Deep Defect States in Narrow Band-Gap Semiconductors,” *Physica B: Condensed Matter* 401-402 (2007): 291–295.

43. D. Liu, H. Yan, X. Yuan, et al., “Thermodynamic Modeling of the Ge–Ti System Supported by Key Experiment,” *Thermochimica Acta* 521, no. 1-2 (2011): 148–154.

44. S. P. Ashburn, M. C. Öztürk, J. J. Wortman, G. Harris, J. Honeycutt, and D. M. Maher, “Formation of Titanium and Cobalt Germanides on Si (100) Using Rapid Thermal Processing,” *Journal of Electronic Materials* 21, no. 1 (1992): 81–86.

45. J. Pelleg, R. Eliahu, A. Barkai, and G. Levi, “A Note on the Reactions in the Ti-Ge System,” *AIP Advances* 2, no. 3 (2012): 032185.

46. The International XPS Database, https://xpsdatabase.net/titanium-ti-z22-chemicals.

47. A. G. Shard, “Detection Limits in XPS for More than 6000 Binary Systems Using Al and Mg Kα X-Rays,” *Surface and Interface Analysis* 46, no. 3 (2014): 175–185.

48. K. C. Phillips, H. H. Gandhi, E. Mazur, and S. K. Sundaram, “Ultrafast Laser Processing of Materials: A Review,” *Advances in Optics and Photonics* 7, no. 4 (2015): 684.

49. M.-J. Sher, N. M. Mangan, M. J. Smith, et al., “Femtosecond-Laser Hyperdoping Silicon in an SF $_6$ atmosphere: Dopant Incorporation Mechanism,” *Journal of Applied Physics* 117, no. 12 (2015): 125301.

50. L. Jiang, A.-D. Wang, B. Li, T.-H. Cui, and Y.-F. Lu, “Electrons Dynamics Control by Shaping Femtosecond Laser Pulses in Micro/Nanofabrication:Modeling, Method, Measurement and Application,” *Light, Science & Applications* 7, no. 2 (2018): 17134.

51. N. Medvedev, Z. Li, and B. Ziaja, “Thermal and Nonthermal Melting of Silicon under Femtosecond X-Ray Irradiation,” *Physical Review B* 91, no. 5 (2015): 054113.

52. A. Rousse, C. Rischel, S. Fourmaux, et al., “Non-Thermal Melting in Semiconductors Measured at Femtosecond Resolution,” *Nature* 410, no. 6824 (2001): 65–68.

53. Z. Chen, H. Ning, and X. Zhang, “Spatial Distribution Characteristics of Plumes Induced by Femtosecond Laser Ablation of Silicon in Vacuum,” *Scientific Reports* 13, no. 1 (2023): 6623.

54. G. Odachi, R. Sakamoto, K. Hara, and T. Yagi, “Effect of Air on Debris Formation in Femtosecond Laser Ablation of Crystalline Si,” *Applied Surface Science* 282 (2013): 525–530.

55. X. Liu, B. Radfar, K. Chen, T. P. Pasanen, V. Vähänissi, and H. Savin, “Tailoring Femtosecond-Laser Processed Black Silicon for Reduced Carrier Recombination Combined with >95% Above-Bandgap Absorption,” *Advanced Photonics Research* 3, no. 4 (2022): 2100234.

56. C. J. Glassbrenner and G. A. Slack, “Thermal Conductivity of Silicon and Germanium From 3°K to the Melting Point,” *Physical Review* 134, no. 4A (1964): A1058–A1069.

57. W. C. Dash and R. Newman, “Intrinsic Optical Absorption in Single-Crystal Germanium and Silicon at 77°K and 300°K,” *Physical Review* 99, no. 4 (1955): 1151–1155.

58. J. Tauc, A. Abrahám, R. Zallen, and M. Slade, “Infrared Absorption in Amorphous Germanium,” *Journal of Non-Crystalline Solids* 4 (1970): 279–288.

59. P. Mc Kearney, S. Schäfer, S. Paulus, et al., “Ultrafast Laser Heating for Controlling the Optoelectronic Properties of Sulfur Hyperdoped Black Silicon,” *Journal of Applied Physics* 133, no. 1 (2023): 013102.

60. O. Salihoglu, U. Kürüm, H. Gul Yaglioglu, A. Elmali, and A. Aydinli, “Femtosecond Laser Crystallization of Amorphous Ge,” *Journal of Applied Physics* 109, no. 12 (2011): 123108.

61. X. Liu, “Highly Strained Ge Nanostructures and Direct Bandgap Transition Induced by Femtosecond Laser,” *Semiconductor Science and Technology* 40, no. 4 (2025): 045013.

Supporting Information

Additional supporting information can be found online in the Supporting Information section.